Heliyon 11 (2025) e41415

Contents lists available at ScienceDirect

Heliyon

journal homepage: www.cell.com/heliyon

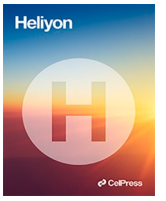

Research article

The photo-electrocatalytic property of hollow mesoporous graphene oxide/tungsten trioxide/titanium dioxide membrane photo-anode

Yuan Li [a], Xinying Sun [a], Jiajia Chen [a], Shuping Luo [a,b,c], Guohua Li [a,b,c,*]

[a] College of Chemical Engineering, Zhejiang University of Technology, China
[b] State Key Laboratory of Green Chemistry Synthesis Technology, China
[c] Key Laboratory of Green Chemistry-Synthesis Technology of Zhejiang Province, Hangzhou, 310032, China

ARTICLE INFO

Keywords:
Titania
Tungsten trioxide
Graphene oxide
Hollow mesoporous structure
Membrane photo-anode
Photo-electrocatalytic property

ABSTRACT

Titania (TiO_2) is one of promising photo catalysts for its high ability to resistant photo corrosion and environmental friendliness, but its photocatalytic activity is too low to be used in industry. To find an approach to solve this problem, graphene oxide (GO), tungsten trioxide (WO_3) and TiO_2 composite with hollow mesoporous structure was prepared by a two-step spray drying method. The composite was used as raw material to constitute a membrane onto ITO glass to form a membrane photo-anode. In this way, its photo-electrocatalytic property was tested. The morphology, crystal phase, microstructure and specific surface area of the composite were characterized by SEM, XRD, TEM and BET, respectively. The surface potential distribution and optical property of the anode were measured by a Kelvin Probe Force Microscopy and a Fs-5 Steady-State Fluorescence Spectrometer, respectively. The forbidden bandwidth of the GO-WO_3/TiO_2 composite is 2.30 eV, which is much lower than that of the WO_3/TiO_2 composite, 2.92 eV. When the content of GO in the anode is around 1 wt%, its light absorption ability is the best among all the anodes with different contents of GO, and its photocatalytic ability to degrade methyl orange is the strongest as our experiments concerned. These findings indicate that the addition of GO into the WO_3/TiO_2 composite can improve its photo-electrocatalytic property. The construction of membrane photo-anode is an efficient approach to solve the problem of the recovery and secondary utilization of nanoscale powder in water treatment.

1. Introduction

Semiconductor photocatalytic technology can directly convert inexhaustible solar energy into chemical energy with a pollution-free manner at room temperature, this can alleviate simultaneously two major problems: energy crisis and environmental pollution. Its reaction process is mostly carried out at room temperature and ordinary pressure, so it is considered as the most ideal clean energy production and environmental governance technology [1–7]. Semiconductor photo-electrocatalytic technologies containing both advantages of photocatalysis and electrocatalysis have attracted a lot of attention in recent years. A bias voltage can facilitate a photocatalytic reaction through the effective separation of the photo-induced electron-hole pairs excited from semiconductor [8–10]. This result from a synergistic effect between photocatalysis and electrocatalysis of the semiconductor has attracted much attention all

* Corresponding author. College of Chemical Engineering, Zhejiang University of Technology, Hangzhou 310032, China.
E-mail address: nanozjut@zjut.edu.cn (G. Li).

https://doi.org/10.1016/j.heliyon.2024.e41415
Received 19 June 2024; Received in revised form 10 December 2024; Accepted 20 December 2024
Available online 20 December 2024

over the world.

Titanium dioxide (TiO_2) is considered as one of the most promising photocatalysts with application prospect for its superior dielectric effect, good chemical stability, and environmental friendliness [11–18]. However, its low utilization rate of sunlight, high recombination rate of photo-induced electron-hole pairs, and difficulty for its recycling and reusing, need to be overcome as concerned in practical application [19–22]. Therefore, how to expand its adsorption range for sunlight, suppress its recombination rate of photo-induced electron-hole pairs, and create an approach for its effective recycling and reusing are interesting and valuable topics in recent years. The WO_3/TiO_2 composite with a hetero-junction structure between WO_3 and TiO_2 can expand the spectral response range of TiO_2 under the irradiation of sunlight [23], facilitate its transport of photo-induced electrons and holes between different energy levels, contribute to its effective separation of photo-induced carriers, improve its photocatalytic efficiency, and exhibit good photocatalytic activity under the irradiation of sunlight [24–27]. However, because of the poor conductivity of WO_3 and TiO_2, the transportation of photo-induced electrons and holes is hindered between two them. Therefore, it is necessary and valuable to find an approach to solve this problem, and to facilitate its efficient separation of photo-induced carriers.

Graphene oxide (GO) has excellent mechanical and electrical properties. And as one of carbon materials with large specific surface area and strong affinity, its oxygen-containing surface functional groups can adsorb pollutant effectively and facilitate the efficient transfer of photo-induced carriers [28–30]. Inspired by these, WO_3/TiO_2 composites with hollow mesoporous structure and large specific surface area were fabricated according to the process reported in reference [31]. After modified by GO, the composites were used as raw materials to prepare membrane photo-anodes onto ITO to test their photo-electrocatalytic properties. And the enhancement of the photo-electrocatalytic ability of the composites modified by GO, and the relationship between their microstructure and photo-electrocatalytic property were reported for the first time. Furthermore, a novel approach to improve the photo-electrocatalytic property of the GO-WO_3/TiO_2 composite, and recover and reuse nanoscale powders during a photo-electrocatalysis was proposed.

2. Experimental

2.1. Fabrication of WO_3/TiO_2 composite

5 g of titanyl sulfate, 2.8 g of ammonium metatungstate (AMT) and appropriate amount of citric acid were added into deionized water at room temperature to get a muddy liquid. The liquid was stirred sufficiently to dissolve all the titanyl sulfate to get a clear solution. A suitable amount of ammonia water ($NH_3 \cdot H_2O$) was added dropwise into the solution to adjust its pH value to 7 while stirring at a speed of 500 $r \bullet min^{-1}$, and then the solution was put aside statically for another 12 h. After that, the solution was sent into a spray-dryer at an inlet temperature of 200 °C, a solution flow of 800 $mL \bullet h^{-1}$ and an air pressure of 0.35 MPa. In this way, the precursor of TiO_2/WO_3 powder was fabricated, and put into a thermostatic box resistance furnace to be calcined at 500 °C for 2 h to get TiO_2/WO_3 composite. The temperature of the precursor, 500 °C, and its content of WO_3, 5 % molar percentage, were set according to reference 31, in which the excellent property of WO_3/TiO_2 composite was reported.

2.2. Preparation of graphene oxide (GO)

GO was prepared by a modified Hummers' method. In detail, 20 mL of phosphoric acid and 180 mL of sulfuric acid were added into a clean round-bottom flask under a cryogenic water bath. The mixed acidic solution was stirred in the flask for 30 min at first, and 1.5 g of graphite powder was added into the solution and stirred for another 30 min to get a dispersion liquid, then 9.0 g of potassium permanganate was slowly added into the liquid while stirring. After that the temperature of the liquid was adjusted to 35 °C and stayed at this temperature for 30 min while stirring, then the temperature was raised to 50 °C and kept at this temperature for 12 h while stirring, and 150 mL of ice water was slowly added into the liquid to stop reaction. Finally, 3–4 mL 30 % H_2O_2 was added until the liquid in the flask turned golden brown. After put it aside statically for 12 h, the liquid was washed and settled with dilute hydrochloric acid at a concentration of 10 wt%. In this way, liquids containing different amounts of GO were gotten, and GO dispersions were obtained by centrifuging the precipitate of the liquids at a high-speed, and washing the GO dispersions with dilute hydrochloric acid (10 wt% concentration) for six times (until the supernatant pH = 5).

2.3. Preparation of GO-WO_3/TiO_2 composite

1 g of the WO_3/TiO_2 composite and a corresponding amount of GO dispersion were added into deionized water to get a suspension. After stirring ultrasonically for 30 min, the pH of the suspension was adjusted to 7 with dilute ammonia water at a concentration of 3.0 wt%. Then it was spray dried at an inlet temperature of 200 °C, a material flow of 800 $mL \bullet h^{-1}$ and an air pressure of 0.35 MPa. In this way, GO-WO_3/TiO_2 composites with different graphene oxide contents, 0.5 wt%, 1.0 wt%, 1.5 wt% and 2.0 wt%, were prepared.

2.4. Preparation of membrane photo-anode

Firstly, an ITO conductive glass ultrasonically cleaned with dish soap, acetone, ethanol, and deionized water for 10 min step by step, and then dried naturally. A suitable amount of WO_3/TiO_2 or GO-WO_3/TiO_2 composites was mixed homogeneously with an appropriate amount of N-methylpyrrolidone and polyvinylidene fluoride in a mortar, and then it was ground evenly to get a homogeneous slurry. The slurry was coated onto the ITO conductive glass by a scraping and coating method to get a membrane photo-anode.

The anode was dried at room temperature, and then placed in a thermostatic box resistance furnace to be calcined at 200 °C for 2 h.

2.5. Characterization

The crystal structures of the membrane photo-anodes were tested by X 'PertPro X-ray diffractometer (PANalytical Company). During the testing process, X-ray source was Cu Kα ray ($\lambda = 0.154056$ nm), tube current was 40 mA, tube voltage was 40 kV, and step size was 0.04°. Their morphologies were observed using a Hitachi S-4700 II field emission scanning electron microscope. Their microstructures and crystal plane spacings were characterized using a Tecnai G2 model F30 high resolution transmission electron microscope. Their Kelvin probe force microscopy (KPFM) was performed using a Nanoscope V Multimode 8 scanning probe microscope (Bruker Corporation). Raman spectroscopy was performed to obtain information about the vibration modes of its molecules. Their specific surface areas and pore size distributions were measured by ASAP2020 automatic physiochemical adsorption instrument (Micrometrics Company) with N_2 adsorption medium at 77 K. Fs-5 Steady-State Fluorescence Spectrometer was used to investigate the recombination of photo-generated carriers. Their diffuse reflectance spectra were obtained in UV2550 UV–visible spectrophotometer (SHIMADZU Company) with $BaSO_4$ white powder as a substrate.

2.6. Photocatalytic activity

The photoelectric conversion properties of the membrane photo-anodes were measured with a three-electrode system, in which the anode was used as work electrode, a platinum plate was used as counter electrode and a saturated calomel electrode was used as reference electrode. A 250 W single-hole xenon lamp was used as a light source to irradiate the anode after being filtered by a leaf of 400 nm to get rid of UV light. During the measurement, a sodium sulfate (Na_2SO_4) aqueous solution at a concentration of 0.5 mol•L^{-1} was used as electrolyte. A bias voltage of 0.5 V was applied during transient photocurrent test.

The measuring process of the photocatalytic property of the anode is almost the same as that of photoelectric conversion property. Methyl orange (MO) solution at a concentration of 10 mg•L^{-1} was used as a simulated pollution. The photo-electrocatalysis was carried out under a bias voltage of 0.5 V. After a defined interval of light irradiation, 3 mL of the solution was fetched to measure its absorption photo-spectrum with a UV–vis spectrophotometer, and according to the relationship between absorbance and solution concentration, the relationship obeys the Bougue-Lambert-Beer law, the degradation rate (η) of MO can be estimated from the absorbance change of MO solution: $\eta\ (\%) = 1\text{-}\ (c/c_0) = 1\text{-}\ (A_t/A_0)$, where c is the immediate concentration of the solution degraded for a defined time (t); c_0 is the initial concentration of MO solution; A_0 is the initial absorbance of the solution; A_t is the immediate absorbance of the solution degraded for a defined time (t) under the irradiation of a light wavelength of 464 nm. According to the final value of c/c_0, the photo-electrocatalytic degradation rate of the photoelectric electrode for MO can be evaluated.

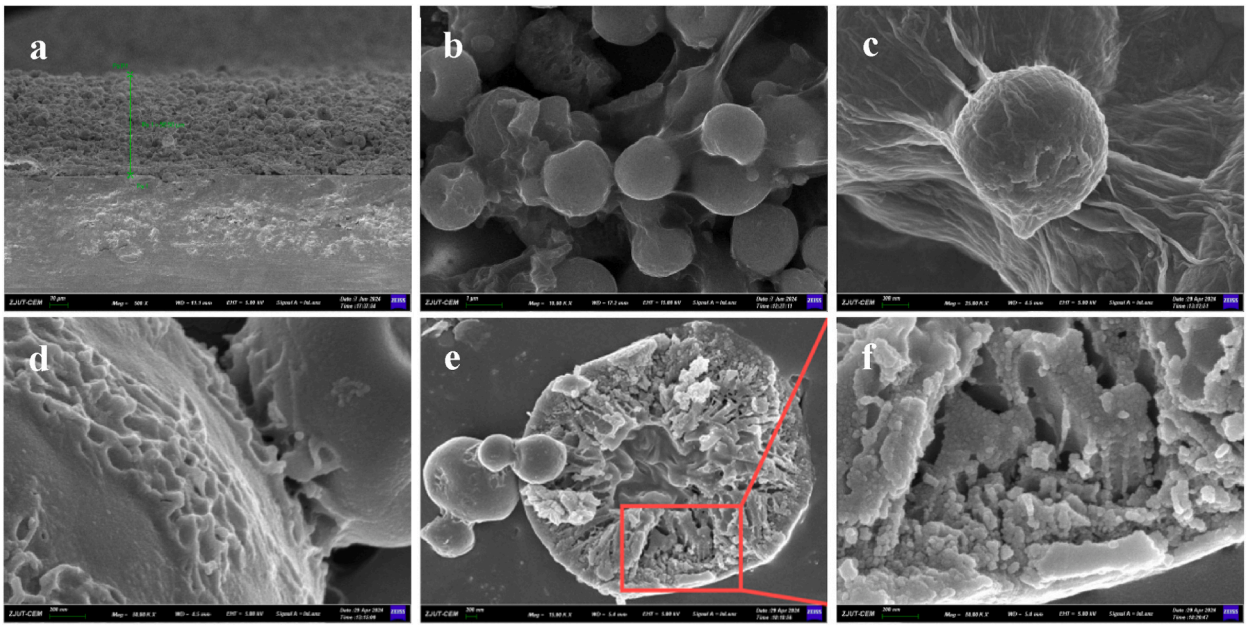

Fig. 1. The SEM images of the GO-WO_3/TiO_2 composite with 1.0 wt% of GO (a) the section of photo-anode; (b) and (c) the morphology of the composite; (d) the surface structure of WO_3/TiO_2 microsphere; (e) and (f) the interior structures of WO_3/TiO_2 microsphere.

3. Results and discussion

3.1. Scanning electron microscopy

Fig. 1 shows the SEM images of 1.0 wt% GO-WO_3/TiO_2 membrane photo-anode. From Fig. 1a, it can be clearly seen the cross-section of the anode. After GO modification, the particle morphology of the GO-WO_3/TiO_2 composite still maintains a regular spherical shape with a diameter ranging from 0.5 to 3.0 μm, as exhibited in Fig. 1b. The surface of the WO_3/TiO_2 microsphere becomes rough, GO distributes on its outer surface and connected different WO_3/TiO_2 microspheres, as shown in Fig. 1c and d. These findings show that GO modifies the surface of WO_3/TiO_2 microsphere successfully. The oxygen-containing functional group of GO can interact with the surface group of the WO_3/TiO_2 microsphere during the spray drying process, resulting in GO disperses and combines tightly on the outer surface of the WO_3/TiO_2 microsphere [33]. The interior structure of the WO_3/TiO_2 microsphere of the anode is shown in Fig. 1e and 1f is a partial enlargement of Fig. 1e. From these two images, one can see it clearly that the structure of the microsphere is hollow with some channels connecting outside space. Furthermore, it is obviously that a mesoporous structure exists in the shell part of the microsphere, as shown in Fig. 1f. Based on these findings, one point can be concluded that the structure of the microsphere is hollow mesoporous.

3.2. Transmission electron microscopy

Fig. 2 shows the TEM images of the GO-WO_3/TiO_2 membrane photo-anode containing 1.0 wt% of GO. From Fig. 2a, it can be clearly seen that the microsphere structure of the anode is porous, the diameter of the microsphere ranges 0.3–0.5 μm, and one material lies between two microspheres and connects them. According to the results of SEM images (Fig. 1c), this material is GO. This finding indicates that GO acts as a bridge between two microspheres and connects them very well in the membrane photo-anode. Fig. 2b shows the enlarged edge of the microsphere, from which more obvious pore structure and the presence of GO on the microsphere edge can be clearly observed. Fig. 2c and d are HRTEM images of the microsphere. From Fig. 2c, the pore structure and the curling phenomenon of

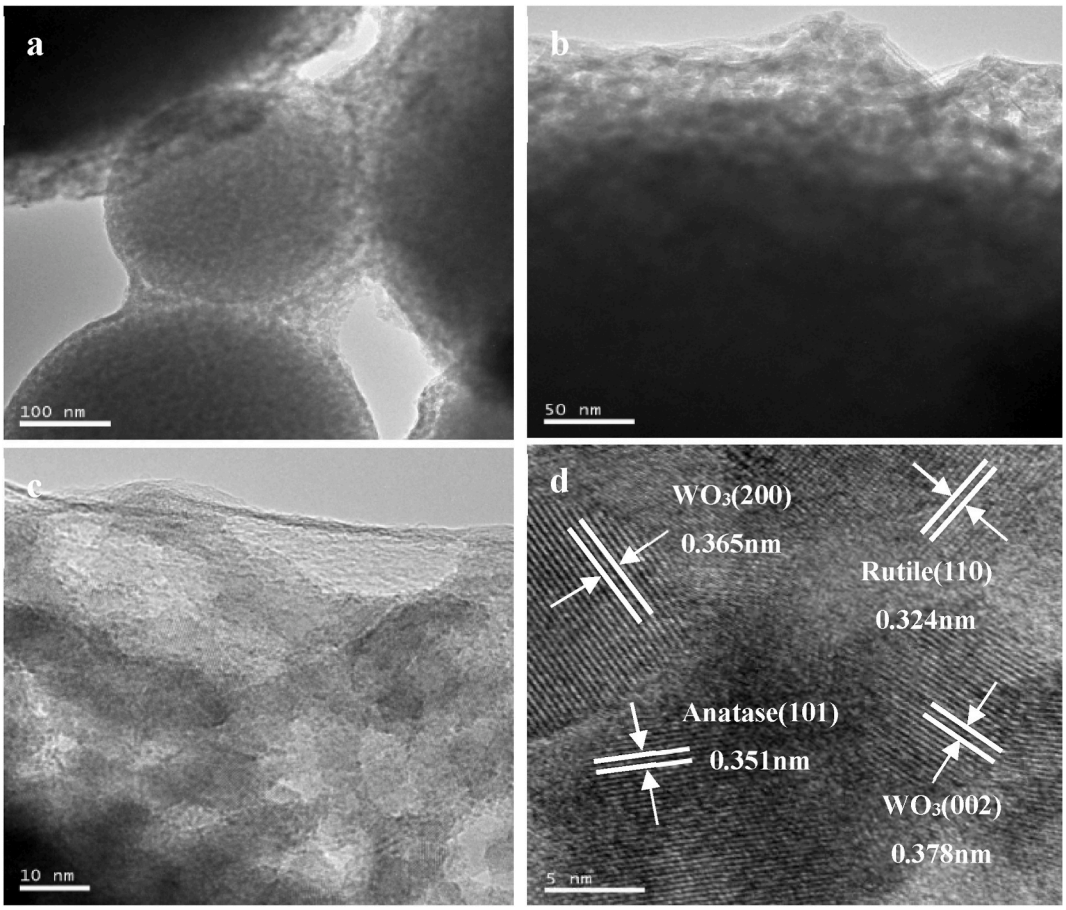

Fig. 2. The TEM images of the GO-WO_3/TiO_2 composite containing 1.0 wt% of GO. (a) morphology; (b) the surface structure of WO_3/TiO_2 microsphere; (c) the local structure of WO_3/TiO_2 microsphere; (d) the lattice spacings of different crystallites.

GO edge can be clearly seen, and some regular lattice fringes can be seen in Fig. 2d, from which two crystal plane spacings, 0.365 nm and 0.378 nm, can be obtained and assigned to the (200) and (002) crystal planes of WO_3, respectively. The crystal plane spacing of 0.351 nm and 0.324 nm can be assigned to anatase (101) and rutile (110) crystal plane, respectively.

Fig. 3 shows the EDS and STEM-EDS Mapping images of the anode containing 1.0 wt% of GO. Fig. 3a shows its EDS analysis results, from which one can see that its chemical elements include Ti, W, O and C, and their average contents are as shown in Table 1. They are selected to make STEM-EDS Mapping pseudo-color maps, and their distributions are shown in Fig. 3b–d. From Fig. 3b and c, it can be clearly seen that the distribution range of element C is basically the same as that of the microsphere, indicating C element distributes uniformly on the outer surface of the WO_3/TiO_2 microsphere. The distribution ranges of O, Ti and W elements are relatively narrow compared with that of the WO_3/TiO_2 microsphere, and are basically consistent with its contour as shown in Fig. 3d and e, respectively. These findings demonstrate that the material at the edge of the microsphere is GO, coating the outer surface of the WO_3/TiO_2 microsphere. These results are consistent with the SEM results. The result of XRF shows the purity of 1.0 wt% GO-WO_3/TiO_2 composite in S-Fig. 2.

3.3. Kelvin probe force microscopy

Fig. 4 shows the height sensor images and corresponding potential curves of KPFM at different sites of the GO-WO_3/TiO_2 membrane photo-anode containing 1 wt% of GO. The AFM images of the anode at different sites are shown in Fig. 4a, b and 4c, and the section curves of the surface potential along the lines as symbolized in Fig. 4a, b and 4c are presented in Fig. 4d, e and 4f, respectively. Combined the section curves of the surface potential to their corresponding AFM images, it is obviously that the brighter area corresponds to higher potential, while the darker area corresponds to lower potential. These phenomena can be attributed to electron transfers from high potential to low potential, which results in photo-induced electrons transfer from brighter area to darker area. These findings demonstrate that photo-induced electrons transfer from WO_3/TiO_2 to GO, enhancing the separation of the photo-induced carriers and prolonging their life-time effectively.

3.4. X-ray diffraction

Fig. 5a shows the XRD patterns of 1.0 wt% GO-WO_3/TiO_2 composite. The diffraction peaks at $2\theta = 23.2°$, 23.7° and 24.4° in the XRD curve of the composite can be attributed to the (002), (020) and (200) crystal planes of WO_3 (PDF 01-072-1465), respectively. The diffraction peaks at $2\theta = 25.4°$, 37.9° and 48.3° can be assigned to the (101), (004) and (200) crystal planes of anatase (PDF 01-089-4921), respectively, and that at $2\theta = 27.1°$, 36.0°, 54.2° can be attributed to the (110), (101) and (211) crystal planes of rutile (PDF 01-076-0318), respectively.

The XRD patterns of GO-WO_3/TiO_2 composites with different contents of GO are shown in S-Fig. 1, in which the diffraction peak at $2\theta = 9.8°$ on the XRD curve of GO can be attributed to the (002) crystal plane of GO [32]. The diffraction peaks of GO-WO_3/TiO_2 composites with different contents of GO are almost the same as those of the WO_3/TiO_2 composite. This finding shows that the crystal

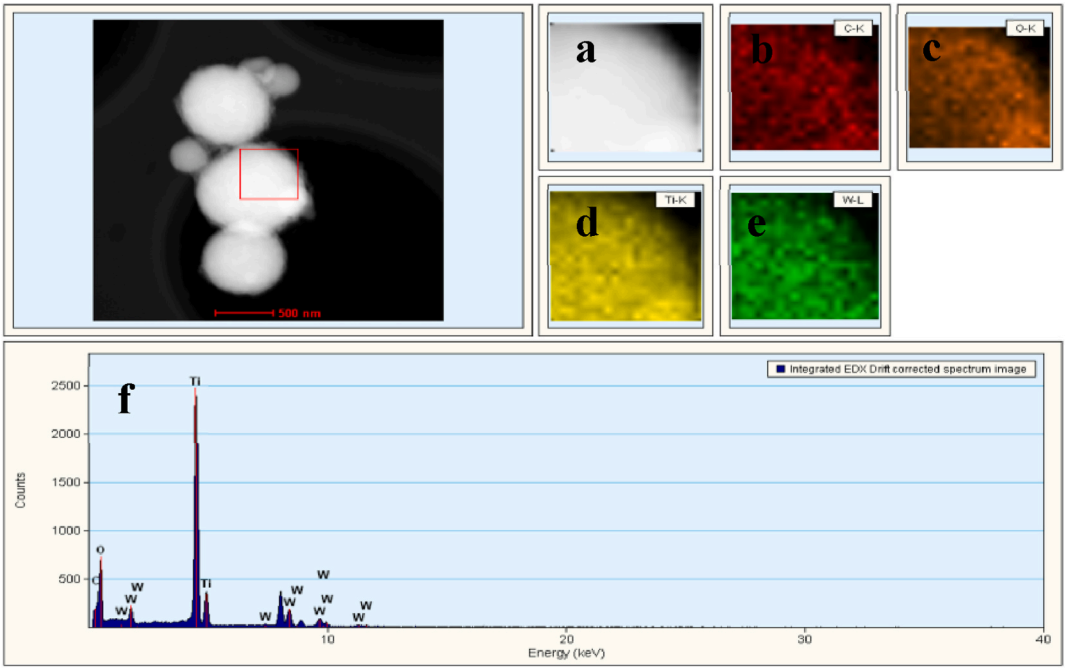

Fig. 3. The STEM-EDX (a) Mapping (b–f) images of the GO-WO_3/TiO_2 composite containing 1.0 wt% of GO.

Table 1
The elements content (at %) of the composite gained form EDS analysis.

Composite	O (at %)	C (at %)	Ti (at %)	W (at %)
1.0 wt% GO-WO_3/TiO_2	50.44	29.07	19.51	0.97

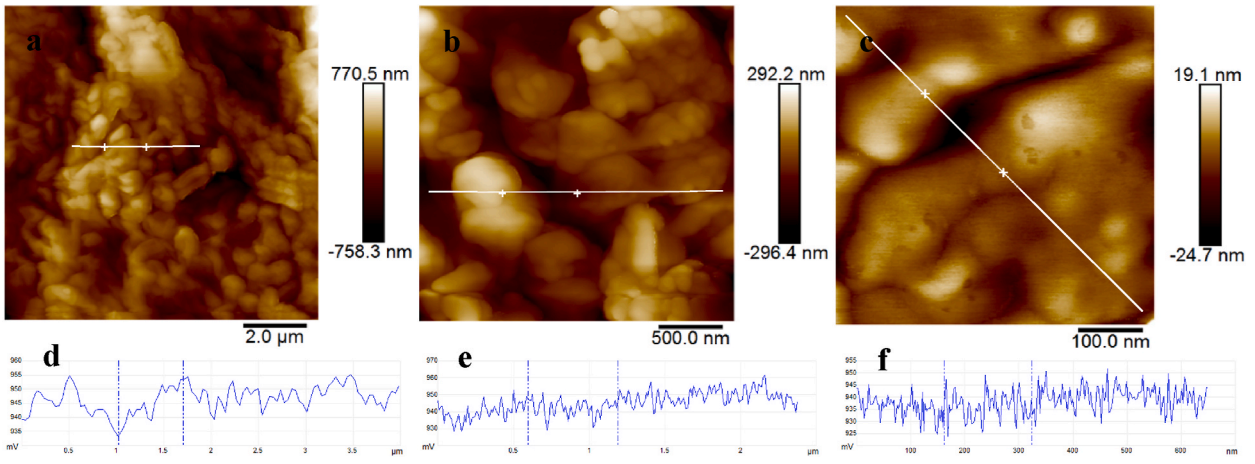

Fig. 4. The AFM images (a, b, c) and corresponding potential curves (d, e, f) of KPFM of the GO-WO_3/TiO_2 composite containing 1.0 wt% of GO.

phases of WO_3 and TiO_2 in the composite do not change significantly after GO modification. Moreover, there is no obvious GO diffraction peak can be observed in the XRD patterns of the composites. This phenomenon may be related to the fact that the GO modified by spray dried is uniformly dispersed on the outer surface of WO_3/TiO_2 microsphere at 200 °C, and its small layer thickness does not exhibit diffraction. The average diameter of the crystalline in the composite can be estimated according to Scherrer Formula: $D = K{\cdot}\gamma/(\beta{\cdot}\cos\theta)$, in which D is the average diameter of crystal; K is the Scherrer constant; γ is the X-ray wavelength; β is the half-height width of a corresponding diffraction peak; θ is the Bragg diffraction angle. Based on the above formula, the average diameter of the crystallite particles in all samples was estimated in nanometers. The results are shown in S-Table 1.

3.5. Raman spectra

The Raman spectra of the WO_3/TiO_2 and GO-WO_3/TiO_2 composites are displayed in Fig. 5b, in which the absorption peaks in the curve of the WO_3/TiO_2 microsphere at 391 cm^{-1}, 516 cm^{-1} and 636 cm^{-1} are correspond to the characteristic vibration peaks of B1g, A1g and E2g of anatase, respectively. The absorption peak at 806 cm^{-1} corresponds to the characteristic vibration peak of the O-W-O bond of WO_3. From Fig. 5b, one can see clearly that the characteristic absorption peaks of TiO_2 and WO_3 in the curve of the GO-WO_3/TiO_2 composite are basically the same as that of the WO_3/TiO_2 composite, and their absorption peaks at 1346 cm^{-1} and 1596 cm^{-1} can be attributed to the D and G peaks of GO. Generally, the intensity ratio of peak D to peak G (I_D/I_G) is used to measure the defect degree in carbon materials [32]. Accordingly, the I_D/I_G ratios of the GO-WO_3/TiO_2 composites containing 0.5 and 1.0 wt% of GO can be estimated, and are 1.44 and 1.27, respectively. The decreasing of the I_D/I_G ratio of the composites indicates the percentage decreasing of carbon atom with sp^3 hybridization in graphene, and the increasing of the graphitization degree in the composites [33]. This implies

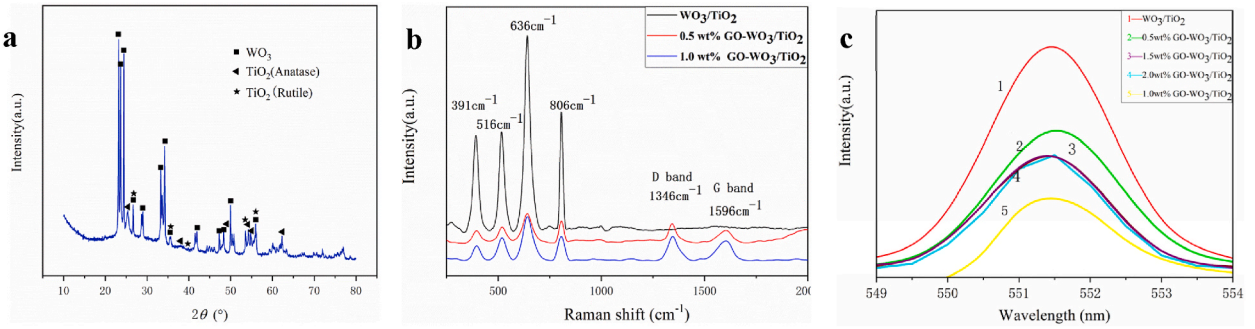

Fig. 5. The XRD patterns of the 1.0 wt% GO-WO_3/TiO_2 composite (a); Raman spectra of WO_3/TiO_2 and GO-WO_3/TiO_2 composites with different contents of GO (b); Fluorescence emission curves of GO-WO_3/TiO_2 composites with different contents of GO (c).

that the graphitization degree is larger for the GO-WO_3/TiO_2 composite containing 1.0 wt% of GO. These findings imply that partial GO in the composite containing 1.0 wt% of GO graphitized, resulting in a decrease of GO compared to the initial amount added for the formation of the composite. It also can be seen from Fig. 5b that the curve of the GO-WO_3/TiO_2 composite drops sharply compared with that of the WO_3/TiO_2 composite. This can be attributed to the absorption effect of GO on the microsphere surface of the composites.

3.6. PL spectra

To investigate the charge-transfer property of the GO-WO_3/TiO_2 membrane photo-anode, its PL spectra are obtained and shown in Fig. 5c. When GO was added in the anode, the PL intensity was reduced significantly. This can be explained by a change in the bandgap after the addition. In this case, GO acts as an electron-hole transition site and effectively facilitates the transfer of photo-induced electron from the valence band of TiO_2 to its conduction band [35]. Thus, the separation rate of photo-induced electron and hole is effectively enhanced and their direct recombination is inhibited. As can be seen from Fig. 5c, as the percentage of GO increases, the fluorescence intensity of the GO-WO_3/TiO_2 anodes decrease firstly and then increase. These findings indicate that the recombination rate of photo-induced electron-hole pairs decrease firstly and then increase. In detail, when the percentage of GO in the anode is 1 wt%, its fluorescence intensity is the lowest. This finding indicates that its optical property is the best among all the anodes with different GO contents.

3.7. XPS spectra

XPS spectra of 1 wt% GO-WO_3/TiO_2 composite is shown in Fig. 6, which providing its chemical state, type, composition and element chemical combined-states [36]. All binding energies conducted in the XPS experiments are trued by referencing C1s peak. From Fig. 6a, one can see it clearly that four elements, C, Ti, W and O, exist in the composite, which is consistent with EDS and XRD results. The main peaks of C 1s are resolved and can be fitted into three peaks, including C-C &C=O&C-H (284.40 eV), C-O (286.21 eV) and O-C=O (288.20 eV), as shown in Fig. 6b [37]. Fig. 6c is the Ti 2p deconvolution spectrum of the composite, and the peaks situated at 458.45 eV and 464.14 eV are ascribed to Ti $2p_{3/2}$ and Ti $2p_{1/2}$, which confirm the presence of Ti^{4+} [38] in the composite. The two peaks at W $4f_{7/2}$ and W $4f_{5/2}$ are agreement with the spin-orbit splitting of W 4f, and they are distributed at 35.35 eV and 37.18 eV, separately (Fig. 6d), suggesting that the main chemical state of W in the photocatalysts is hexavalent [39]. Fig. 6e shows the XPS spectrum of O 1s, in which four chemical bonds can be fitted. The peaks around 530.20 eV and 531.45 eV are ascribed to Ti-O and W-O bonding, while the peak at 529.57 eV represents W-O-Ti bond. The binding energy of 532.34 eV is ascribed to C-O bond [36,40]. These findings demonstrate that W-O-Ti bonds and WO_3/TiO_2 heterojunctions exist in the GO-WO_3/TiO_2 composite.

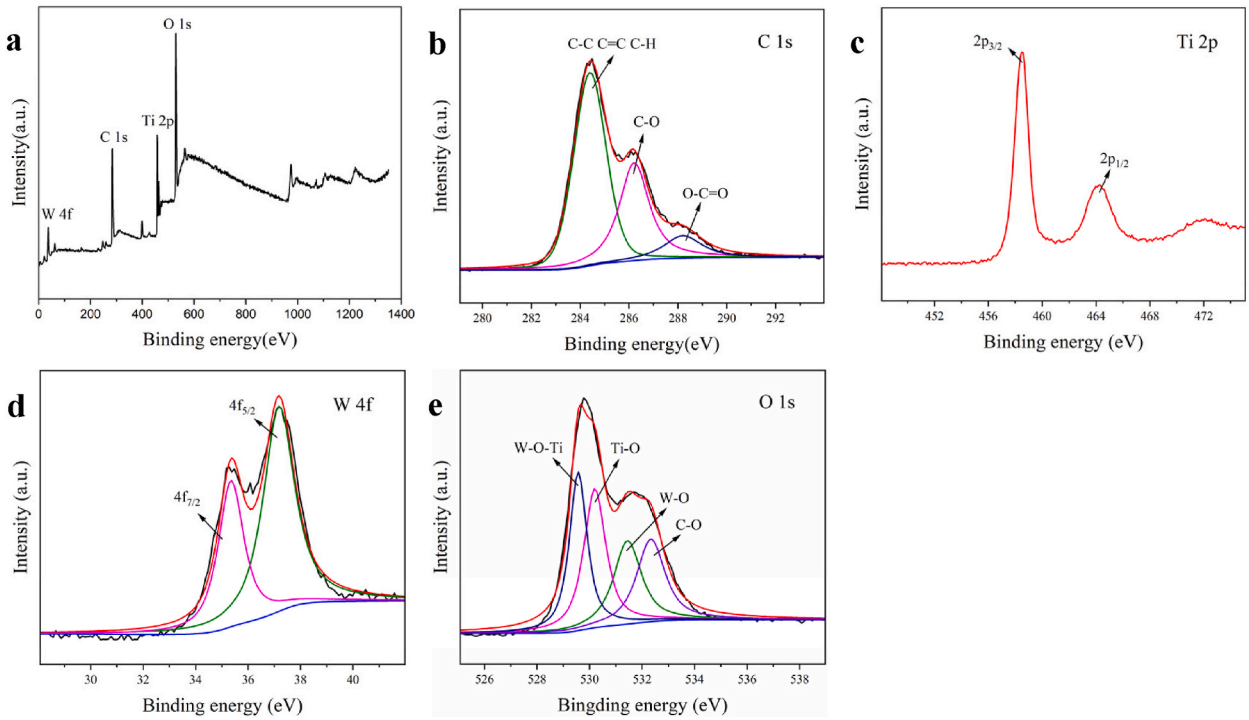

Fig. 6. The XPS spectra of 1 wt% GO-WO_3/TiO_2 composite
(a) whole spectrum of the composite; (b) C 1s; (c) Ti 2p; (d) W 4f; (e) O 1s.

3.8. BET analysis

The N_2 adsorption-desorption isotherms of the WO_3/TiO_2, 0.5 wt% GO-WO_3/TiO_2 and 1.0 wt% GO-WO_3/TiO_2 composites are shown in Fig. 7, in which the slope of the curves is gentle and the adsorption amount of gas is small in its low-pressure area, while in its high-pressure area, obvious H2 hysteresis loops can be seen. It is generally believed that the existence of H2 hysteresis loops is caused by porous adsorbent or uniform particle accumulation holes, which indicates that the porosity of the composites are interstitial pore formed by the nanoparticle accumulation of the composites. In the high-pressure area of the WO_3/TiO_2 composite, both H2 and H4 hysteresis loops can be seen, as shown in Fig. 7a; while in that of the GO-WO_3/TiO_2 composite, no H4 hysteresis loops are observed, as shown in Fig. 7b and c. This can be attributed to the modification of the microstructure of WO_3/TiO_2 composite after the addition of GO on the surface of the WO_3/TiO_2 microspheres, as shown in the SEM image in Fig. 2c.

The distributions of the pore sizes in the composite membranes are shown in the inserts in Fig. 7. The pore sizes range from 2 to 35 nm with an average size around 5 nm, as shown in Table 1. This indicates that the composites are mesoporous. The BET specific surface areas of 0.5 and 1.0 wt% GO-WO_3/TiO_2 composites are 66.6 and 80.7 $m^2\ g^{-1}$, respectively, which are bigger than that of WO_3/TiO_2 composite (58.8 $m^2\ g^{-1}$), as shown in Table 2. The enlargement of its specific surface area can not only improve its adsorption property, but also provide more active sites to enhance its catalytic property [34].

3.9. UV–vis diffuse reflection spectra

Fig. 8a shows the diffuse reflection spectra of the WO_3/TiO_2 and GO-WO_3/TiO_2 composites, and Fig. 8b shows their forbidden band widths converted according to the corresponding "Kubelka-Munk" formula [41]. As can be seen from Fig. 8a, all the samples have stronger absorption in UV region, while relatively weaker absorption in visible region. The absorption intensity of the WO_3/TiO_2 composite is the weakest among all the composites; as the increases of GO in the GO-WO_3/TiO_2 composites from 0.5 wt% to 1.0 wt%, their absorption intensities increase in visible region. When their GO percentages increase from 1.0 wt% to 1.5 wt%, their absorption intensities decrease in visible region. Finally, as the increasing of GO further from 1.5 wt% to 2.0 wt%, their absorption intensities increase again in visible region. The absorption intensity of the composite containing 1.0 wt% of GO is the strongest in visible region among the composites with different contents of GO, as our experiments concerned. These results indicate that the content of GO in GO-WO_3/TiO_2 affects the absorption, as the absorption peak exhibits red and blue shifts depending on the GO content. This may be due to the combination of GO with semiconductor, indicating that a certain degree of chemical interaction occurs between semiconductor and GO, resulting in the formation of M − C or M-O-M-(M represents metal) chemical bond on the surface, or even at a certain depth near the interface between GO and semiconductor [42]. This kind of bond is like carbon doping into semiconductor, introducing energy levels and consequently leading to the narrowing of the energy band gap of the semiconductor. This causes a certain degree of red shift extending the response range to visible light [43]. As can be seen from Fig. 8b, the forbidden bandwidth of the WO_3/TiO_2 composite is 2.92 eV, while that of the GO-WO_3/TiO_2 composites is related to their content of GO. When their contents of GO are 0.5 wt %, 1.0 wt%, 1.5 wt% and 2.0 wt%, their forbidden band widths are 2.88, 2.30, 2.71 and 2.82 eV, respectively. These findings indicate that as the increasing of GO content, their forbidden band widths decrease at first and then increase. Based on the above findings, one point can be concluded that the content of GO in the composites has a great influence on their absorptive ability for light, and its appropriate content is around 1.0 wt%.

3.10. Photocatalytic performance under visible light irradiation

The transient photocurrent responses curves of the membrane photo-anodes with different GO contents are shown in Fig. 9, from which the photocurrent densities of the anodes with different contents of GO, 0.0, 0.5, 1.0, 1.5 and 2.0 wt%, are 20.8, 27.0, 48.0, 40.0, 33.0 and 24.0 μA•cm^{-2}, respectively. The order of their photocurrent density is 1.0 wt% GO-WO_3/TiO_2>1.5 wt% GO-WO_3/TiO_2>2.0 wt% GO-WO_3/TiO_2>0.5 wt% GO-WO_3/TiO_2>WO_3/TiO_2, indicating that the addition of GO into the anodes can enhance significantly their photocurrent response, while their photocurrent densities increase at first and then decrease as the increasing of GO content.

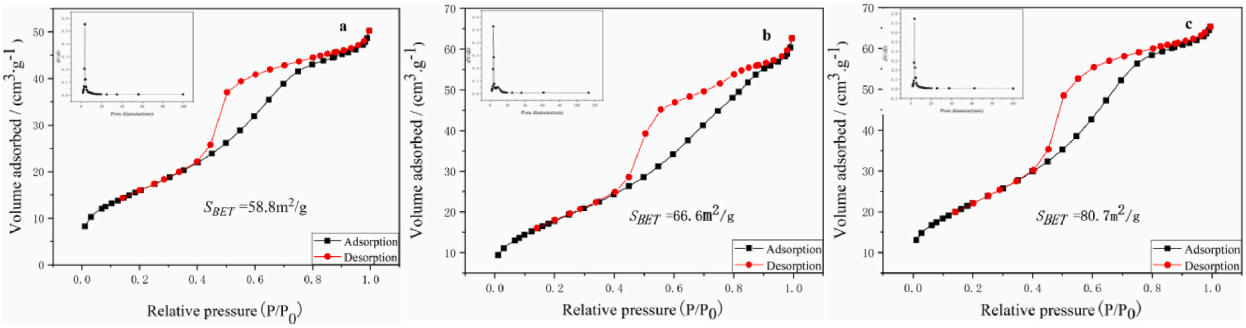

Fig. 7. The N_2 adsorption–desorption isotherms and the corresponding pore size distribution of GO-WO_3/TiO_2 composites with different contents of GO. (a) 0.0 % (WO_3/TiO_2); (b) 0.5 wt%; (c) 1.0 wt%.

Table 2
The BET results of WO_3/TiO_2 and GO-WO_3/TiO_2 composites.

Sample	$A_{BET}/m^2/g$	Average diameter/nm
WO_3/TiO_2	58.8	5.0
0.5 wt% GO-WO_3/TiO_2	66.6	5.4
1.0 wt% GO-WO_3/TiO_2	80.7	4.8

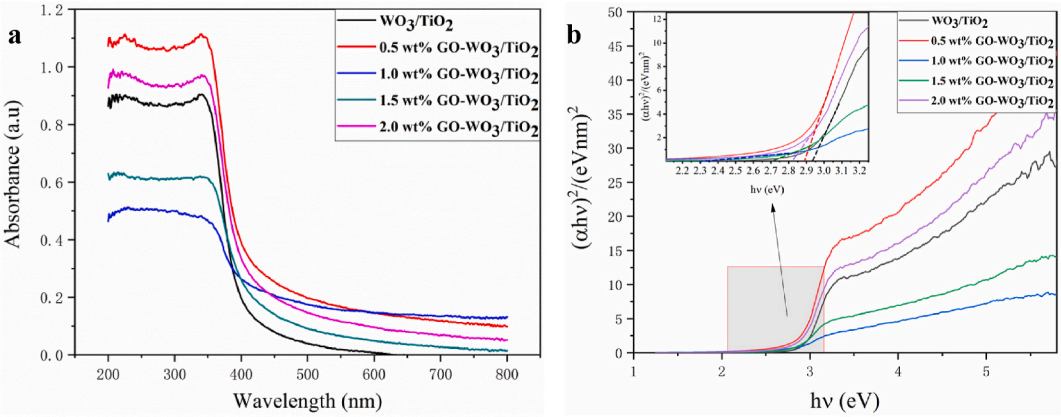

Fig. 8. The UV–vis diffuse reflectance spectra (a) and the curves of forbidden bandwidth (b) of the composites.

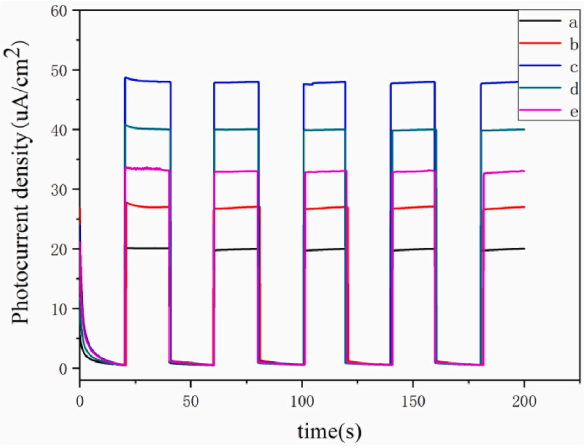

Fig. 9. The transient photocurrent of the GO-WO_3/TiO_2 membrane photo-anodes with different contents of GO (a) 0.0 % (WO_3/TiO_2); (b) 0.5 wt%; (c) 1.0 wt%; (d) 1.5 wt%; (e) 2.0 wt%.

These findings imply that an appropriate amount of GO added in the anode can effectively promote its separation rate and utilization rate of photo-induced carriers, thus improving its photocurrent response.

The photo-electrocatalytic degradation of MO by the membrane photo-anodes with different contents of GO under sunlight irradiation is shown in Fig. 10a. It can be observed that when the anodes containing 0.0, 0.5, 1.0, 1.5 and 2.0 wt% of GO, their photo-electrocatalytic degradation rates for MO are 39.6 %, 44.1 %, 70.3 %, 65.4 %, 54.8 %, respectively, under the irradiation of stimulated sunlight for 120 min. Moreover, during the photo-electrocatalytic degradation process, GO-WO_3/TiO_2 membrane photo-anodes with different GO contents are stable in MO solution and do not fall off at least after five consecutive repetitions of the experiment. These findings indicate that the order of their photo-electrocatalytic activity is 1.0 wt% GO-WO_3/TiO_2>1.5 wt% GO-WO_3/TiO_2>2.0 wt% GO-WO_3/TiO_2>0.5 wt% GO-WO_3/TiO_2>WO_3/TiO_2. The order is consistent with that of the transient photocurrent responses (Fig. 9). This can be attributed to the fact that when the content of GO exceeds a certain amount it becomes a recombination center for photo-induced electrons and holes resulting in a low photo-electrocatalytic degradation [42].

According to reference [44], the degradation reaction of TiO_2 for low-concentration dyes conforms to the first-order kinetic process: $\ln(c_0/c) = k \bullet t$ (where c_0 and c represent the concentrations of MO in the degradation liquid at initial time and time t, respectively, and t is the reaction time; k is the reaction rate constant). The kinetic curves of the photocatalytic degradation for MO in

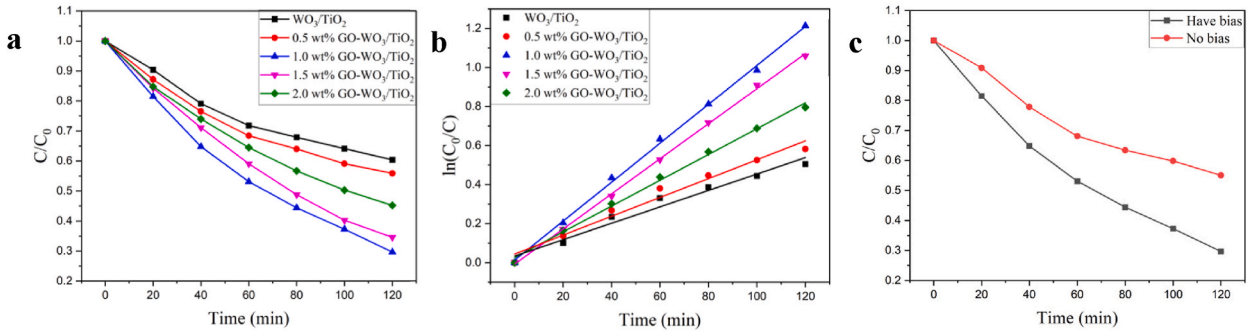

Fig. 10. The photo-electrocatalytic degradation for methyl orange by the membrane photo-anodes with different contents of GO under the irradiation of sunlight (a) and their corresponding degradation kinetics (b); Effect of bias voltage (c) on the photo-electrocatalytic degradation of 1 wt% GO-WO_3/TiO_2 membrane photo-anodes for methyl orange.

the presence of different samples were shown in Fig. 10b, from which one can see it clearly that $\ln(c_0/c)$ has a linear relationship with time t, indicating the degradation of MO obeys to a first-order kinetic process. The k (min^{-1}) values for WO_3/TiO_2, 0.5 wt% GO-WO_3/TiO_2, 1.0 wt% GO-WO_3/TiO_2, 1.5 wt% GO-WO_3/TiO_2 and 2.0 wt% GO-WO_3/TiO_2 composites are 0.00420 min^{-1}, 0.00482 min^{-1}, 0.00997 min^{-1}, 0.00899 min^{-1} and 0.00660 min^{-1}, respectively. These findings show that the photocatalytic activity of 1.0 wt % GO-WO_3/TiO_2 composite is the highest among all the samples.

The effect of bias voltage on the photo-electrocatalytic degradation efficiency of the anode with 1.0 wt% of GO is shown in Fig. 10c. It can be seen clearly that under the irradiation of stimulated sunlight for 120 min, when no bias added, its photocatalytic degradation rate is 44.9 % only; when the external bias applied, its photo-electrocatalytic degradation rate increases to 70.3 %. These findings indicate that the catalytic performance of the anode increase nearly 56.6 % when a bias voltage of 0.5 V is applied. It can be attributed to the fact that electrons move along the external circuit easily, efficiently, and stably under voltage bias during photo-electrocatalysis, which may be due to the presence of GO between two WO_3/TiO_2 microspheres and acts as a bridge between them, as shown in Fig. 2. This can promote the separation rate of photo-induced electron and hole pairs [4], thus enhance the yield of photo-induced hole and hydroxyl radical, and resulting in the improvement of photo-electrocatalytic efficiency.

3.11. Discussion

The formation mechanism of the hollow porous structure of the microsphere by spray drying process can be summarized as followings: the solution containing titanyl sulfate ($TiOSO_4$) and ammonium metatungstate (AMT) is stable under the aids of a suitable amount of citric acid (CA) and ammonia water ($NH_3{\cdot}H_2O$), as shown in Fig. 11a; when the solution was sent into the spray-dryer, its droplets are in full contact with the hot air, the temperature of the droplets increased rapidly, and the surface water, CA and $NH_3{\cdot}H_2O$ evaporates, at this time, $TiOSO_4$ hydrolyzes, resulting TiO_2 formation, and AMT presents as crystallite, as shown in Fig. 11b; as the water evaporating from the droplet, the TiO_2 and AMT crystallite contact with each other, resulting the formation of hollow microsphere, as shown in Fig. 11c; in this case, when the concentrations of $TiOSO_4$ and AMT are high enough, more and more TiO_2 and AMT crystallite aggregate from the inner to outer of the droplet, resulting the thickness increase of the hollow microsphere, as shown in Fig. 11d; when the hollow microsphere was calcined, the AMT in the hollow microsphere decomposes, resulting the evaporation of NH_3 and formation of WO_3, and the formation of mesopore in the microsphere, thus increases its porosity, as shown in Fig. 11e.

The comparison of the degradation efficiency between the GO-WO_3/TiO_2 membrane photo-anode and other similar photocatalysts reported in the literature are listed in Table 3. From Table 3, one can see it clearly, when compared to C-TiO_2/WO_3 photocatalyst [45], the GO-WO_3/TiO_2 membrane photo-anode exhibits a higher degradation efficiency, even though both have similar structure; when compared to TiO_2/WO_3/GO photocatalyst [36], though its structure and catalytic performance are similar to that of the GO-WO_3/TiO_2 membrane photo-anode, but its practical application effect is relatively low for it was irradiated by UV-light, whose energy is higher than visible light's. The TiO_2 (001)/GO nanocomposite reported in reference 46 exhibits a better degradation performance, but its band gap is relatively wide, a light with a higher energy is needed to excite it. That's the reason why LED lamp was used as a light source in reference 46. Because the wavelength of LED lamp is 450–460 nm, which is shorter than that MB can absorb maximum, and the light energy of LED lamp is 2.70–2.76 eV, which is higher than the band gap (3.13 eV) of the TiO_2 (001)/GO nanocomposite reported in reference 46, resulting in electron-hole pairs can be excited from the composite much easily, thus enable it to exhibit higher degradation performance. The TiO_2 (001)/GO nanocomposite reported in reference 47 display a similar degradation performance with the GO-WO_3/TiO_2 membrane photo-anode, but its band gap is relatively low. In addition, both TiO_2 (001)/GO nanocomposites are difficult to recycle for secondary use. Based on the above results and discussions, one point can be concluded that the GO-WO_3/TiO_2 membrane photo-anode has a higher photo-degradation efficiency and a better promising future in industrial application.

The improvement of the photocatalytic activity of the GO-WO_3/TiO_2 membrane photo-anode can be ascribed to the synergistic effect of two facts: a) The formation of the WO_3/TiO_2 junction, and b) its modification by adding GO. The formation of the WO_3/TiO_2 expands the range of the response spectrum. Under the irradiation of sunlight, photo-induced electrons in the conduction band of TiO_2 tend to transfer into that of WO_3, and a lot of positively charged holes in the valence band of WO_3 will transfer into that of TiO_2 at the

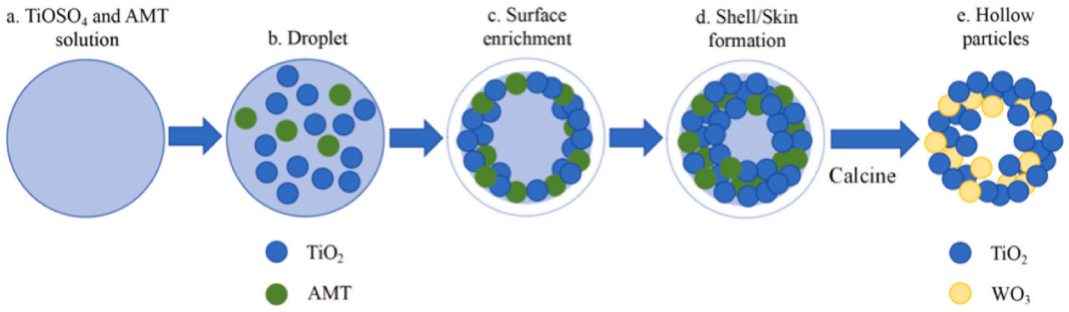

Fig. 11. The mechanism of hollow particles by spray drying process.

Table 3
The comparison of the photocatalytic activity of different photocatalysts.

Photocatalyst	Light	Solution	Degradation rate	Reaction rate constant(min^{-1})	Eg(eV)	Reference
C-TiO_2/WO_3	Visible light	MB	54.00 % 3 h	3.50×10^{-3}	/	[45]
TiO_2/WO_3/GO	UV-light	MO	74.00 % 2 h	/	2.32	[36]
TiO_2 (001)/GO	LED Lamp	MB	95.00 % 0.2 h	324.70×10^{-3}	3.13	[46]
TiO_2 (001)/GO	Visible light	MB	51.30 % 1 h	12.40×10^{-3}	2.72	[47]
GO-WO_3/TiO_2	Visible light	MO	70.30 % 2 h	9.97×10^{-3}	2.30	This work

same time. Thus, the photo-induced electron and hole can transfer across the interface between WO_3 and TiO_2 in different directions as shown in Fig. 12. Thus, the presence of the heterojunction leads to a reduction of recombination rate of the photo-induced electron-hole pairs. According to the results of SEM, TEM, STEM-EDS Mapping and KPFM of the GO-WO_3/TiO_2 composite, GO distributes on the outer surface of the WO_3/TiO_2 microspheres, acting as a bridge between different microspheres, connecting them, as shown in Fig. 12. On one hand, as the conductivity of GO is excellent, the GO bridge can facilitate the transportation of the photo-induced electrons from the conduction band of TiO_2 to that of WO_3, and promote the separation rate of the photo-induced carriers effectively. On the other hand, the addition of GO can increase the specific surface area of the anode and improve its adsorption ability. Furthermore, the GO-WO_3/TiO_2 composite, fabricated by a two-step spray drying method, has hollow mesoporous structure, enabling adsorption of larger amounts of pollutant molecules, which can diffuse to the surface of the microspheres by the chemical potential, thus resulting in a higher concentration of pollutant molecules around the active sites of the electrode during photo-electrocatalysis. This increases the photo-electrocatalytic efficiency of the membrane electrode for the degradation of the pollutant molecules.

4. Conclusions

The GO-WO_3/TiO_2 composites with hollow mesoporous structures are successfully prepared by a two-step spray drying method, and are coated onto ITO conductive glass by a scraping and coating method to form a membrane photo-anode. The membrane photo-anode of the GO-WO_3/TiO_2 composite exhibits excellent photo-electrocatalytic activity under the irradiation of sunlight. An external voltage bias can promote the separation rate of photo-induced electron-hole pairs, and improve the catalytic performance of the anode

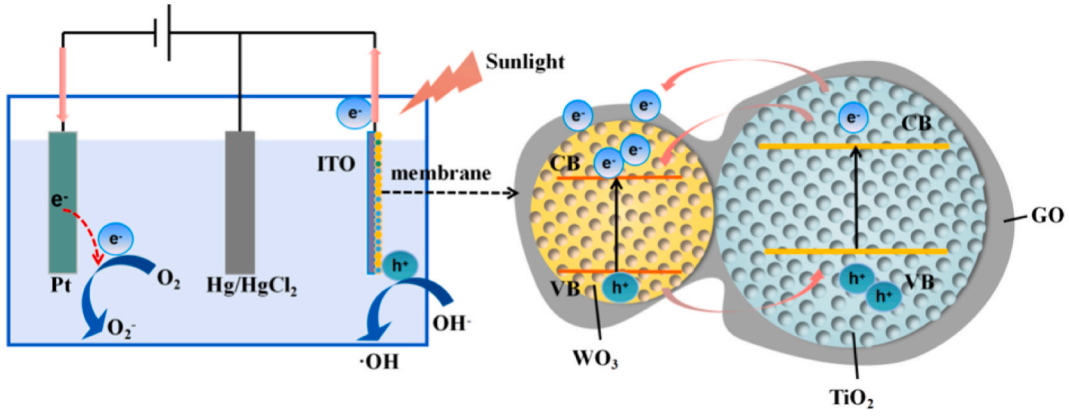

Fig. 12. The schematic illustration of the mechanism for the degradation improvement of the hollow mesoporous GO-WO_3/TiO_2 membrane photo-anode.

near 56.6 %. WO_3 composited with TiO_2 can improve the photocatalytic activity of the WO_3/TiO_2 membrane photo-anode synergistically for a heterojunction structure formed between WO_3 and TiO_2, thus reducing the recombination rate of electron-hole pairs. GO modifies the outer surface of WO_3/TiO_2 microspheres and connects them closely, enhancing the transportation of photo-induced electrons from the conduction band of TiO_2 to that of WO_3 along GO easily and efficiently. Furthermore, the addition of GO can increase the specific surface area and improve the concentration of pollutant molecules around the active sites of the WO_3/TiO_2 composite, and facilitate the photo-electrocatalytic process. GO modification is a promising approach to enhance the photo-electrocatalytic activity of GO-WO_3/TiO_2 composite, and membrane photo-anode is a promising approach to recycle and reuse nanoscale powder in water treatment and can be exploited in industrial application.

CRediT authorship contribution statement

Yuan Li: Writing – original draft, Methodology, Investigation. **Xinying Sun:** Investigation, Formal analysis, Data curation. **Jiajia Chen:** Methodology, Formal analysis. **Shuping Luo:** Writing – original draft, Supervision. **Guohua Li:** Writing – review & editing, Supervision, Methodology, Funding acquisition.

Data statement

All relevant data are within the manuscript and its additional files.

Declaration of competing interest

The authors declare that they have no known competing financial interests or personal relationships that could have appeared to influence the work reported in this paper.

Acknowledgments

This work was supported by the National Key Research and Development Program of China (No.2022YFC2904804), Engineering Research Center of Non-metallic Minerals of Zhejiang Province (No. ZD2023K05) and Zhejiang University of Technology Transverse research project (No. KYY-HX-20190025 and KYY-HX-20230192).

References

[1] M. Umer, I.A. Hussein, A. Al-Ahmed, S. Ahmed, IEEE J of PHOTOVOLT 6 (2016) 486–490, https://doi.org/10.1109/jphotov.2016.2514703.
[2] W.Z. Cui, J. Ma, K.Z. Wu, J. Chen, M.X. Wu, Int. J. Electrochem. Sci. 12 (2017) 11487–11495, https://doi.org/10.20964/2017.12.72.
[3] M. Tahir, B. Tahir, N.A.S. Amin, H. Alias, Appl.Surf.Sci. 389 (2016) 46–55, https://doi.org/10.1016/j.apsusc.2016.06.155.
[4] S. Noor, R.S. Haider, S. Noor, S. Sajjad, S.A.K. Leghari, M. Mehboob, M. Long, Int.J.Hydrogen.Energ. 47 (2022) 36517–36529, https://doi.org/10.1016/j.ijhydene.2022.08.207.
[5] Z. Yousaf, S. Sajjad, S.A.K. Leghari, S. Noor, A. Kanwal, S.H. Bhatti, K.H. Mahmoud, Z.M. El-bahy, J. Environ. Chem. Eng. 9 (2021) 106716, https://doi.org/10.1016/j.jece.2021.106746.
[6] D. Gu, B.H. Wang, Y.J. Zhu, H.J. Wu, Aust. J. Chem. 69 (2015) 343–348, https://doi.org/10.1071/ch15484.
[7] J.J. Hu, C.Y. Ma, J.L. Wang, C. Leng, F.W. Qin, Q.Y. Zhang, Chinese J.Inorg.Chem. 36 (2020) 2240–2248, https://doi.org/10.11862/CJIC.2020.241.
[8] W.K. Yu, M. Xu, X. Liang, J.Y. Wang, W.Y. Fang, F.W. Wang, Chemosphere 313 (2023) 137591, https://doi.org/10.1016/j.chemosphere.2022.137591, 2023.
[9] Y.B. Xie, L.M. Zhou, H.T. Huang, Mater. Lett. 60 (30) (2006) 3558~3560, https://doi.org/10.1016/j.matlet.2006.03.058.
[10] L. Valenzuela, M. Faraldos, A. Bahamonde, R. Rosal, Electrochim. Acta 395 (2021) 139–203, https://doi.org/10.1016/j.electacta.2021.139203.
[11] Q. Guo, C.Y. Zhou, Z.B. Ma, X.M. Yang, Adv. Mate. 31 (50) (2019) SI, https://doi.org/10.1002/adma.201901997.
[12] S. Shamaila, A.K.L. Sajjad, F. Chen, J.L. Zhang, Catal. Today 175 (2011) 568–575, https://doi.org/10.1016/j.cattod.2011.03.041.
[13] S. Noor, S. Sajjad, S.A.K. Leghari, C. Flox, S. Ahmad, J. Environ. Sci. 108 (2021) 107–119, https://doi.org/10.1016/j.jes.2021.02.009.
[14] P. Sasanka, B.D.S. Haritha, N.R. Kumudu, V.B. Sanjaya, R.P. Ishanie, J. Chin, Chem. Soc-Taip 68 (5) (2021) 738–769, https://doi.org/10.1002/jccs.202000465.
[15] B. Han, X.J. Li, Z.M. Zhang, H.Y. Wang, K.F. Yu, C. Liang, Nanotechnology 33 (2021) 035704, https://doi.org/10.1088/1361-6528/ac2d4a.
[16] Y.J. Gu, M. Zhou, Z.H. Dong, Z.Q. Cheng, T.S. Deng, JPCS 1885 (6) (2021) 032012, https://doi.org/10.1088/1742-6596/1885/3/032012.
[17] W.Y. Ko, T.C. Wu, S.Y. He, K.J. Lin, Nanotechnology 35 (2024) 175403, https://doi.org/10.1088/1361-6528/ad22aa.
[18] Z Alsheheri Soad, Shawky Ahmed, T Alsaggaf Wejdan, Z.I. Zaki, Nanotechnology 33 (2022) 305701, https://doi.org/10.1088/1361-6528/ac6816.
[19] X.F. Li, X.F. Wu, S.W. Liu, Y.H. Li, J.J. Fan, K.L. Lv, Chinese J.Catal. 41 (10) (2020) 1451–1467, https://doi.org/10.1016/s1872-2067(20)63594-x.
[20] H.J. Cheng, W.T. Xu, Org. Biomol. Chem. 17 (47) (2019) 9977–9989, https://doi.org/10.1039/c9ob01739a.
[21] X.H. Lin, H. Chen, Z.B. Hub, Y.D. Hou, W.X. Dai, S.S.Sci. 83 (2018) 181–187, https://doi.org/10.1016/j.solidstatesciences.2018.07.007.
[22] H.P. Li, X.S. Dong, B. Sun, G.W. Zhou, J. Mater. Eng. 49 (8) (2021) 54–62, https://doi.org/10.11868/j.issn.1001-4381.2020.000556.
[23] M. Humayun, F. Raziq, A. Khan, W. Luo, Green Chem. Lett. Rev. 11 (2) (2018) 86–102, https://doi.org/10.1080/17518253.2018.1440324.
[24] Q.L. Chen, S.Y. Lou, Y.Q. Wang, S.M. Zhou, Inorg. Chem. Commun. 148 (2022), https://doi.org/10.1016/j.inoche.2022.110307.
[25] V. Iliev, D. Tomova, L. Bilyarska, J.Photoch.Photobio.A 351 (2017) 69–77, https://doi.org/10.1016/j.jphotochem.2017.10.022.
[26] MdM. Rhamana, S. Gangulib, S. Berac, S.B. Rawald, A.K. Chakraborty, J. Water Process Eng. 36 (2020) 101256, https://doi.org/10.1016/j.jwpe.2020.101256.
[27] Q. Wang, W.M. Zhang, X.R. Hu, L.M. Xu, G.D. Chen, X.C. Li, J. Water Process Eng. 40 (2021) 101943, https://doi.org/10.1016/j.jwpe.2021.101943.
[28] S. Sajjad, F. Arshad, B. Uzair, S.A.K. Leghari, S. Noor, M. Maaza, ChemistrySelect 4 (2019) 10365–10371, https://doi.org/10.1002/slct.201902641.
[29] A. Malik, S. Sajjad, S.A.K. Leghari, Y. Naz, M. Masood, I. Ahmad, B. Uzair, Appl. Nanosci. (11) (2021) 1211–1223, https://doi.org/10.1007/s13204-021-01727-5.
[30] S. Shamaila, A.K.L. Sajjad, Q. U-Alin, S. Shaheen, A. Iqbal, S. Noor, G. Sughra, U. Ali, J. Environ. Chem. Eng. 5 (2017) 5770–5776, https://doi.org/10.1016/j.jece.2017.11.009.
[31] G.H. Li, J.J. Chen, S.Z. Wu, Y. Yu, Y. Li, Y.R. Li, J. Gao, Surf.Innov. 6 (1–2) (2017) 37–46, https://doi.org/10.1680/jsuin.17.00039.
[32] Y.Q. Ding, X.Z. Guo, D.L. Kuang, X.F. Hu, Y. Zhou, Y. He, Z.J. Zang, J. Hazard Mater. 416 (2021) 126218, https://doi.org/10.1016/j.jhazmat.2021.126218.
[33] Y.H. Zhang, Z.R. Tang, X.Z. Fu, Y.J. Xu, ACS Nano 5 (9) (2011) 7426, https://doi.org/10.1021/nn202519j.
[34] P.P. Zhang, S. Yang, H.G. Xie, Y. Li, F.X. Wang, M.M. Gao, K. Guo, R.H. Wang, X. Lu, ACS Nano 16 (2022) 17593–17612.

[35] X.M. Liu, T. Xu, Y.L. Li, Z.G. Zang, X.S. Peng, H.Y. Wei, W.Y. Zha, F. Wang, Sol.Energ.Mat.Sol.C. (187) (2018) 249–254, https://doi.org/10.1016/j.solmat.2018.08.009.
[36] X.Y. Hao, M. Li, L. Zhang, J. Ind. Eng. Chem. 55 (2017) 140–148, https://doi.org/10.1016/j.jiec.2017.06.03.
[37] L. Zhang, Q.H. Zhang, H.Y. Xie, J. Guo, H.L. Lyu, Y.G. Li, Z.G. Sun, H.Z. Wang, Z.H. Guo, Appl. Catal. B Environ. 201 (2017) 470–478, https://doi.org/10.1016/j.apcatb.2016.08.056.
[38] Z. Geng, Y. Zhang, X. Yuan, M.X. Huo, Y.H. Zhao, Y. Lu, Y. Qiu, J.Alloy.Compd. 644 (2015) 734–741, https://doi.org/10.1016/j.jallcom.2015.05.075.
[39] J. Lu, Y. Wang, F. Liu, L. Zhang, S. Chai, Appl. Surf. Sci. 393 (2017) 180, https://doi.org/10.1016/j.apsusc.2016.10.003.
[40] M. Nazari, F. Golestani-Fard, R. Bayati, B. Eftekhari-Yekta, Superlattice. Microst. 80 (2015) 91, https://doi.org/10.1016/j.spmi.2014.12.008.
[41] W.J. Ong, L.L. Tan, S.P. Chai, S.T. Yong, A.R. Mohamed, Nano Res. 7 (10) (2014) 1528–1547, https://doi.org/10.1007/s12274-014-0514-z.
[42] W.S. Wang, D.H. Wang, W.G. Qu, L.Q. Lu, A.W. Xu, J. Phys. Chem. C 116 (37) (2012) 19893–19901, https://doi.org/10.1021/jp306498b.
[43] S. Sakthivel, H. Kisch, Angew. Chem. Int. Ed. 42 (2003) 4908–4911, https://doi.org/10.1002/anie.200351577.
[44] X.L. Zheng, D.Q. Zhang, Y. Gao, Y.C. Wu, Q.Y. Liu, X.X. Zhu, Inorg. Chem. Commun. 110 (2019) 107589, https://doi.org/10.1016/j.inoche.2019.107589.
[45] Y.H. Kim, S.Y. Lee, H.N. Umh, H.D. Song, J.W. Han, J.W. Choi, J.H. Yi, ACS.Appl.Mater.Interfaces 12 (13) (2020) 15239–15245. https://pubs.acs.org/doi/10.1021/acsami.0c00669.
[46] A. Izzataddini, Y. Romdoni, Helmiyati, et al., Inorg. Chem. Commun. 157 (2023) 111379, https://doi.org/10.1016/j.inoche.2023.111379.
[47] T.Y. Rika, N.S. Tatya, C.C.D. Lizbeth, et al., J. Phys. Chem. Solid. (2022) 110357, https://doi.org/10.1016/j.jpcs.2021.110357.